

Cancer Cell Membrane Camouflaged Cascade Bioreactor for Cancer Targeted Starvation and Photodynamic Therapy

Shi-Ying Li¹, Hong Cheng¹, Bo-Ru Xie¹, Wen-Xiu Qiu¹, Jing-Yue Zeng^{1,2}, Chu-Xin Li¹, Shuang-Shuang Wan¹, Lu Zhang¹, Wen-Long Liu¹, Xian-Zheng Zhang^{1,2}*

¹Key Laboratory of Biomedical Polymers of Ministry of Education & Department of Chemistry,
Wuhan University, Wuhan 430072, China

²The Institute for Advanced Studies, Wuhan University, Wuhan 430072, China

*Corresponding author: xz-zhang@whu.edu.cn

ABSTRACT: Selectively cut off the nutrients supply and their metabolism pathways of cancer cells would be a promising approach to improve the efficiency of cancer treatment. Here, a cancer targeted cascade bioreactor (designated as mCGP) was constructed for synergistic starvation and photodynamic therapy (PDT) by embedding the glucose oxidase (GOx) and catalase in the cancer cell membrane-camouflaged porphyrin metal organic frameworks (MOFs) of PCN-224 (PCN stands for porous coordination network). Due to the biomimetic surface functionalization, the immune escape and homotypic targeting behaviors of mCGP would dramatically enhance the cancer targeting and retention abilities. Once internalized by cancer cells, mCGP was found to promote the microenvironmental oxygenation by catalyzing the endogenous hydrogen peroxide (H_2O_2) to produce oxygen (O_2), which would subsequently accelerate the decomposition of intracellular glucose and enhance the production of cytotoxic singlet oxygen ($^1\text{O}_2$) under light irradiation. Consequently, mCGP displayed amplified synergistic therapeutic effects of long-term cancer starvation therapy and robust PDT, which would efficiently inhibit the cancer growth after a single administration. This cascade bioreactor would further facilitate the development of complementary modes for spatiotemporally controlled cancer treatment.

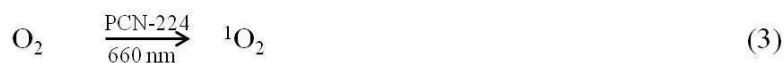
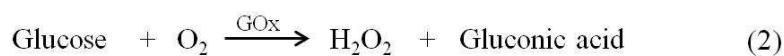
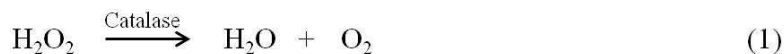
KEYWORDS: metal organic framework, cell membrane, starvation therapy, photodynamic therapy, homotypic targeting

Altering cancer metabolic pathway represents attractive therapeutic targets for cancer targeting therapy.¹⁻⁵ Generally, the abnormal proliferation of cancer cells needs sufficient nutrients and energy supply to support their survival and growth.^{6,7} And the resulting up-regulation of the intracellular aerobic glycolysis, known as Warburg effect,⁸⁻¹¹ would cause cancer cells to become more sensitive to the changes of glucose concentration. Based on this character, a strategy was proposed for cancer starvation therapy by depleting the intratumoral glucose.¹²⁻¹⁴ However, in consideration of the same metabolism requirements of glucose in normal cells, traditional starvation strategies were short of cancer targeting ability, which might induce serious off-target effects.^{15,16} Moreover, the adaptive up-regulation of cancer cells by parallel energy supplies might even lead to the failure of starvation therapy.^{17,18} To amplify the therapeutic effects, a complementary mode was proposed to cut off the cancer glucose supply and destroy the glucose metabolism related cellular elements.^{19,20}

Photodynamic therapy (PDT) is a non-invasive approach for precise ablation of local cancers by the great oxidation abilities of reactive oxygen species (ROS) to nucleic acids, enzymes and cellular membranes.²¹⁻²⁴ However, photosensitizers (PSs) often need to be transformed into pharmaceutical formulations due to their limited solubility.²⁵⁻³¹ Even so, the low loading efficiency as well as the premature leaking behaviors would further limit their applications.³²⁻³⁶ Recently, nano-sized porphyrin metal organic frameworks (nMOFs) were fabricated as nanophotosensitizers (nanoPSs) for PDT with the advantages of facile diffusion of singlet oxygen ($^1\text{O}_2$), avoidable self-quenching and high PSs loading.³³⁻³⁶ However, the hypoxic nature of the cancer microenvironment, caused by the rapid proliferation of cancer cells and distorted cancer blood vessels, was highly detrimental to the oxygen (O_2)-dependent PDT.³⁷⁻⁴¹ In addition, nanoPSs could not evade the immune system and they were short of specific targeting, which would further reduce their therapeutic efficiency and cause systemic side effects.

Traditionally, surface modifications of nanoparticles with polymers and targeting ligands could improve the blood circulation time and enhance the cancer targeting ability.⁴²⁻⁴⁴ However, the complex synthesis as well as the possibility of activating the immune system would greatly restrict their general applicability.⁴⁵⁻⁴⁷ Moreover, the receptor density and its selective recognition would also reduce the targeting efficiency. As we know, cancer cells possessed some particular features such as immune escape and homologous binding, which were tightly associated with their plasma membrane proteins.⁴⁸⁻⁵⁰ Recently, a versatile approach was developed for biomimetic delivery by coating the nanoparticles with natural cell membranes.⁵¹⁻⁵⁷ The superficially camouflaged cell membranes could complete the replication of surface antigenic diversity of the source cells, endowing nanoparticles with immune escape and homotypic targeting abilities.⁵⁸⁻⁶⁵ Also, this top-down approach would extensively simplify the processes for the multifunctional decoration of nanoparticles.⁶⁶⁻⁶⁹

In this paper, a cancer cell membrane-camouflaged cascade bioreactor was constructed for cancer targeted starvation therapy and PDT. As illustrated in Scheme 1, porphyrin based Zr-MOF of PCN-224 was employed as nanoPSs, which also served as the carrier to load glucose oxidase (GOx) and catalase. Finally, the GOx and catalase loaded PCN-224 was further coated with cancer cell membrane to obtain the bioreactor of mem@catalase@GOx@PCN-224 (short as mCGP). Benefiting from the immune escape and homotypic targeting abilities of cancer cell membrane, mCGP would prefer to accumulate at the cancer tissues and selectively internalize into cancer cells. It was found that, the cascade reactions of mCGP could promote the catalysis of the endogenous hydrogen peroxide (H_2O_2) to produce O_2 , accelerate the decomposition of glucose and enhance the production of cytotoxic 1O_2 upon light irradiation based on following equations:



Here, catalase could not only modulate cancer hypoxia microenvironment by catalyzing the decomposition of endogenous H_2O_2 [Equation (1)], but also reduce the O_2 consumption along with the decomposition of glucose by GOx [Equation (2)]. Moreover, the generated O_2 could also enhance the production of highly toxic ${}^1\text{O}_2$ [Equation (3)], which would further improve the therapeutic efficiency by synergistic starvation therapy and PDT. Consequently, the amplified synergistic effects of long-term cancer starvation therapy and robust PDT would efficiently inhibit the cancer growth in a spatiotemporal controlled manner.

RESULTS AND DISCUSSION

Synthesis and Characterization of mCGP. PCN-224 was synthesized according to the literature reports.³⁴ In brief, tetrakis (4-carboxyphenyl)porphyrin (TCPP), $\text{ZrOCl}_2 \cdot 8\text{H}_2\text{O}$ and benzoic acid were dissolved in N,N-dimethylformamide (DMF) and stirred at 90 °C for 5 h. The morphology of as-synthesized PCN-224 was observed by scanning electron microscopy (SEM) (Figure 1A) and transmission electron microscopy (TEM) (Figure 1B), indicating its monodispersed size distribution at about 105 nm. And the obtained PCN-224 also exhibited a narrow hydrodynamic size distribution at 118.5 nm (Figure 1D) and a positive charge potential at 24.5 mV (Figure 1E). Subsequently, GOx and catalase were loaded onto PCN-224 (CGP) by the electrostatic interactions and the loading efficiency calculated by BCA Protein Assay Kit was 13.5 % (Figure S1), which was also consistent with thermo gravimetric analyzer (TGA) observations (Figure S2). After loading, it was found that the particle size of PCN-224 (118.5 nm) increased to about 152.8 nm (Figure 1D) and its zeta potential (24.5 mV) reversed to nearly -10.3

mV (Figure 1E), which verified the successful adherence of GOx and catalase onto PCN-224. To prepare mCGP, CGP was further cloaked with murine mammary carcinoma (4T1) cancer cell membrane fragments by extruding from the polycarbonate porous membrane. In contrast to PCN-224 with naked spherical structures (Figure 1B), mCGP exhibited an obvious core-shell structure with uniform outer lipid bilayer shell of about 10 nm in thickness (Figure 1C), demonstrating the successful cloaking of cancer cell membrane. Moreover, the hydrodynamic particle size of the obtained mCGP also increased to about 227.5 nm (Figure 1D) and the charge potential decreased to nearly -20.9 mV (Figure 1E). Of special note, the hydrodynamic size distribution, the polydispersion index (PDI) and the zeta potential of mCGP were almost constant in 7 days, which confirmed its good stability in stock solution (Figure 1F and Figure S3, S4). Besides, no obvious difference was found in powder X-ray diffraction (PXRD) patterns between mCGP and PCN-224 (Figure 1G), indicating that mCGP retained the same crystal structure and crystallinity with PCN-224. Additionally, the protein ingredient of mCGP was analyzed by using sodium dodecyl sulfate-polyacrylamide gel electrophoresis (SDS-PAGE). It was observed that the cancer cell membrane proteins were extensively reserved and the bands corresponding to catalase (62 kDa) and GOx (80 kDa) were also found in the SDS-PAGE of mCGP (Figure 1H), demonstrating that catalase and GOx were successfully embedded in the cancer cell membrane camouflaged PCN-224. Furthermore, very few of the intracellular biomarkers including Histone H3 (nuclear marker), Cytochrome C (mitochondrial marker), and GAPDH (cytosolic marker) were observed using western blot analysis (Figure S5), indicating the preferential retention of membrane protein. As controls, mem@catalase@PCN-224 (short as mCP) and mem@GOx@PCN-224 (short as mGP) were also prepared and characterized using the same protocols (Figure 1D, E and Figure S6).

Cascade Catalytic Reactions of mCGP. After validating the successful loading of GOx and catalase, their catalytic properties in mCGP were then detected. Above all, the catalytic capabilities of free GOx and catalase were evaluated.⁷⁰⁻⁷² In the presence of O₂, GOx could catalyze the decomposition of glucose to produce gluconic acid with the pH reduction (Figure S7) and the O₂ consumption (Figure S8). Also, the drop in pH was related to both glucose (Figure S9) and GOx (Figure S10) concentrations. Besides, catalase would catalyze the breakdown of H₂O₂ and promote the oxygenation of the microenvironment (Figure S11). Based on these, the cascade catalytic ability of mCGP was evaluated for glucose decomposition and O₂ production (Figure 2A). As illustrated in Figure 2B, the pH values of mCGP solution were kept constant at around 6.4 when without the treatment of glucose. In contrast, due to the glucose decomposition by GOx in mCGP, a dramatic pH drop (from 6.4 to 3.09) happened after treatment with glucose. At the same time, the O₂ concentration also decreased from 5.02 mg/L to 0 mg/L in 500 s (Figure 2C). However, in the presence of H₂O₂, mCGP would accelerate the O₂ production with the concentration increased from 5.02 mg/L to 24.3 mg/L in 500 s due to the breakdown of H₂O₂ by catalase in mCGP. Similarly, the catalytic generation of O₂ by mCGP was also observed in the macroscopic images (Figure S12). These results strongly indicated the catalytic ability of mCGP to decompose glucose and produce O₂.

After that, the cascade ¹O₂ production ability of mCGP was measured using singlet oxygen sensor green (SOSG) as the indicator.^{73,74} As shown in Figure 2D, the SOSG fluorescence increased sharply after treatment with mCGP and irradiation. However, a relatively weak SOSG fluorescence was observed after using NaN₃ as the ¹O₂ quencher, and the SOSG fluorescence kept constant at a low level in the absence of mCGP or light irradiation. These results demonstrated that mCGP could efficiently produce ¹O₂ under light. More specifically, mCGP exhibited an accurate response of ¹O₂ generation to the OFF-ON irradiation (Figure 2E), which could be of

great benefit to precisely control the PDT efficiency according to the personal requirements. It was noteworthy that mCGP could efficiently produce $^1\text{O}_2$ in the presence of H_2O_2 and light (Figure 2F), suggesting the cascade catalytic ability of mCGP to catalyze the formation of O_2 for $^1\text{O}_2$ production. Above results strongly reflected the cascade synergistic effects between catalase, GOx and PCN-224 in mCGP. Taken together, due to the O_2 -dependent characteristics of GOx and PCN-224 for glucose decomposition and $^1\text{O}_2$ production, the cascade reactions of mCGP exhibited great potential to mitigate the cancer hypoxia for improving the starvation therapy and PDT effect by converting the cancer abundant H_2O_2 into O_2 .

Additionally, the ROS production ability of mCGP in living cells were also measured using DCFH-DA as the indicator.⁷⁵⁻⁷⁷ As illustrated in Figure 2G and Figure S13, compared with PCN-224 and TCPP, mCGP exhibited a greater ROS production ability with the higher DCF fluorescence observation. It was worth mentioning that a weak DCF fluorescence was also found after treatment with DCFH-DA only, which confirmed the existence of endogenous H_2O_2 in living cells.⁵² But an attenuated DCF fluorescence was found in 4T1 cells after incubated with mCGP and DCFH-DA, which was ascribed to the catalytic breakdown of endogenous H_2O_2 by mCGP. Also, similar results were demonstrated by the quantitative analysis with flow cytometry (Figure 1H), verifying that mCGP could efficiently produce ROS in living cells, and also convert the endogenous H_2O_2 into O_2 . And this cascade pattern could be also achieved by substituting copper sulfide nanocrystals, $\beta\text{-SnWO}_4$, gold nanocages and quantum dots for PCN-224 as the nanoPSs for enhanced PDT.⁷⁸⁻⁸¹ In addition, in consideration of the interaction of functional materials with glucose and glucose oxidase, the cascade reactions could be extended for many other biological applications. For example, glucose biosensors could be fabricated using glucose oxidase decorated graphene sheets.⁸² The pH drop might be employed for amorphous calcium carbonate and calcium phosphate based drug delivery or cancer imaging.^{83,84} Moreover, the

generated H_2O_2 could be subsequently used for reactive oxygen species-responsive drug delivery or Fenton reaction based cancer therapy.^{85,86} And also, the consumption of O_2 could induce hypoxia of the local environment, which might be employed to amplify the therapeutic effects of bioreductive therapy.⁸⁷

Homotypic Target and Immune Escape Study of mCGP. It had been mentioned before that the surface antigens were responsible for the homologous adhesion nature of cancer cells, and the cancer cell membrane-cloaked platforms was expected to exhibit excellent cancer cell targeting ability.⁵¹⁻⁶⁵ Thus, the homotypic targeting ability of mCGP against 4T1 cells were evaluated using African green monkey kidney (COS7) normal cells as the control. As illustrated in Figure 3A, mCGP preferred to accumulate in 4T1 cells rather than COS7 cells. Similarly, 4T1 cells exhibited 2.8-folds stronger mCGP fluorescence than that of COS7 cells by the quantitative flow cytometry analysis (Figure 3C, D). Additionally, it was also found that mCGP exhibited the relatively weak accumulation in the heterogenous cancer cells of mouse melanoma (B16F10) and human hepatocellular liver carcinoma (HepG2) cells (Figure S14). These results indicated the targeting specificity of mCGP toward 4T1 cells due to its homotypic binding properties. Furthermore, the subcellular locations of mCGP against 4T1 cells were identified using co-location studies with LysoTracker Green and MitoTracker Green. The red fluorescence of mCGP co-localized well with LysoTracker Green (Figure 3H), while it did not match well with the MitoTracker Green (Figure 3G) and Hoechst 33342 (Figure 3A). It could be concluded that mCGP was internalized into 4T1 cells by endocytosis pathway. Moreover, considering that cancer cell possessed immune escape ability owing to the cancer associated antigens and immunological adjuvants on their surface membrane,⁸⁸⁻⁹⁰ the cellular uptake behavior of mCGP against murine macrophages (RAW264.7) was evaluated using PCN-224 as the control. As illustrated in Figure 3B, a large amount of PCN-224 was internalized by the RAW264.7 cells with intense fluorescence

observation. However, a relatively weak fluorescence was observed in RAW264.7 cells after treatment with mCGP. Besides, the obvious difference was also found that PCN-224 exhibited 2.5-folds stronger uptake by RAW264.7 cells than that of mCGP by flow cytometry (Figure 3E) and the mean fluorescence analysis (Figure 3F), demonstrating a good immune escape ability of mCGP.

***In Vivo* Cancer Imaging by mCGP.** Inspired by the superior ability of *in vitro* homotypic targeting and immune escape, the *in vivo* cancer targeting and accumulation behavior of mCGP was further evaluated towards the homologous 4T1 cancer bearing mice. In consideration of the light penetration ability, the absorbance of mCGP at 640 nm was employed for the *in vivo* imaging (Figure S15). As shown in Figure 4A, obvious cancer contrast mCGP fluorescence was observed after intravenous injection for 12 h. And then, the mCGP fluorescence increased steadily until to reach the peak at 48 h. Subsequently, the fluorescence at the cancer site was gradually decreased from 60 h to 96 h, indicating the sustained excretion of mCGP from the cancer tissue. However, no strong fluorescence signal was found in the cancer tissue after administration with PCN-224 (Figure 4B). This dramatic difference might be ascribed to the enhanced immune escape and specific cancer targeting of mCGP endowed by the cancer cell membrane coating. Similar trends were also attested by the *in vivo* cancer imaging analysis that mCGP exhibited a long term cancer retention time and two times higher fluorescence intensity was always found in the cancer of mice with mCGP treatment compared to whose with PCN-224 treatment (Figure 4C, D). Moreover, the semiquantitative analysis of the fluorescence in sacrificed organs and cancer tissues also exhibited the improved cancer accumulation and retention ability after coating with the homotypic cancer cell membrane (Figure 4E, F). Besides, it should be noted that intense fluorescence was also found in lung after treatment with mCGP for 96 h, which might be ascribed to the trapping of mCGP in lung capillaries.^{91,92} To sum up, the

excellent cancer accumulating ability of mCGP should be attributed to the immune escape as well as homotypic targeting abilities of the cancer cell membrane camouflage. Importantly, this highly specific cancer recognition ability of mCGP might extensively enhance the therapeutic effect with little side effects.

In Vitro Synergistic Therapeutic Effects of mCGP. Having verified the excellent targeting ability, the anticancer effect of mCGP was then assessed *in vitro*. Glucose played an important role in cancer cell growth,^{93,94} which could accelerate the proliferation of cancer cells (Figure S16). Reversely, cutting off the intracellular glucose by GOx could inhibit cancer cell proliferation in an O₂ concentration related manner (Figure S17). Moreover, the subsequently generated H₂O₂ could moderately enhance the starvation therapeutic effects, but it might be ineffective (Figure S18). The *in vitro* cytotoxicity of mCGP was then examined against 4T1 cells in 21% O₂ and 2% O₂ atmosphere to mimic the normoxia and hypoxia environment. Above all, the cell viabilities of 4T1 and COS7 cells were measured in the absence and presence of light, demonstrating that the light irradiation was harmless (Figure S19). As controls, the dark toxicities of PCN-224 (Figure S20), catalase (Figure S21) and mCP (Figure S22) were firstly evaluated by MTT assay. As expected, no obvious cytotoxicities were observed, indicating their good biocompatibility. Besides, either in normoxia or in hypoxia environments, mCGP displayed the highest phototoxicity against 4T1 cells (Figure 5A, B), which strongly confirmed the synergistic effects of mCGP by starvation therapy and PDT. As the control, it was also found that mCGP presented both lower dark and light toxicities against COS7 cells than that of 4T1 cells under normoxia environment, which further proved its homotypic target ability (Figure S23). Furthermore, in hypoxia environment, an enhanced anticancer effect was found after treatment with mCGP compared with that of mGP (Figure 5B, C), indicating that catalase played a very important role in the O₂-dependent starvation therapy and PDT [Equation (2) and Equation (3)]

by catalyzing H_2O_2 to generate O_2 . Additionally, the cytotoxicities were also examined by flow cytometry using Annexin V-FITC/PI. As illustrated in Figure 5D, Q1, Q2, Q3 and Q4 represented dead cells, late apoptosis cells, early apoptosis cells and vital cells, respectively. The proportion of dead and apoptosis cells was 6.77%, 10.38% and 19.81% after treatment with mCP, mGP and mCGP in the shield of light, which increased to 29.27%, 34.05% and 38.82% after exposed to light irradiation for PDT. These *in vitro* results further reflected the definite superiority of mCGP for cancer therapy in comparison with the single starvation therapy or PDT. Moreover, the combination of cancer starvation therapy and PDT were secure strategies for cancer treatment due to the up-regulation of the intracellular aerobic glycolysis of cancer cells and light-controlled toxicity of PDT. And also, simultaneously cutting off the cancer cell glucose metabolism by long term starvation therapy and destroying the intracellular elements by robust PDT would be an effectively synergistic strategy for spatiotemporal controlled cancer treatment.

***In Vivo* Anticancer Effects of mCGP.** Then, the *in vivo* anticancer effect was evaluated using 4T1 cancer bearing mice model. Guiding from the results of the *in vivo* and *ex vivo* imaging, mCGP was found accumulated at the cancer site after 12 h post injection and then it would increase gradually until reach the peak at 48 h (Figure 6A). It could be deduced that cancer starvation therapy would happen when the obvious cancer accumulation of mCGP was observed at 24 h and then terminate when mCGP was mostly extracted at 96 h. Furthermore, a robust PDT was implemented at 48 h post injection to achieve the best synergistic effects with cancer starvation therapy. To evaluate the therapeutic efficacy, the anticancer effects of mCGP were systematically investigated *in vivo*. As illustrated in Figure S24, progressively grew of the implanted cancers were observed after treatment with PBS, PBS and light, GOx and catalase or PCN-224 in the following 7 days and 14 days. However, the cancer growth was inhibited to varying degrees after treatment with PCN-224 and light, mCP and light, mGP and light, mCGP,

or mCGP and light. Of particular note, due to the synergistic starvation therapy and PDT, the cancer was completely suppressed after a single treatment with mCGP and light for 14 days (Figure 6B). Furthermore, mCGP exhibited a certain anticancer activity in the absence of light, which was ascribed to the cancer targeting behaviors as well as its long-term starvation therapeutic effects. Moreover, in the presence of light, mGP exhibited a comparable anticancer effect with that of mCP, while both of them still not as good as the collaborative effect of mCGP, indicating that the cascade reactions of mCGP might amplify the starvation therapy and PDT by oxidating the cancer microenvironment. To further prove this hypothesis, immunofluorescence staining of HIF-1 α was carried out to investigate the cancer hypoxia microenvironment. As illustrated in Figure 6F, a reduced HIF-1 α immunofluorescence was observed at the cancer regions after treatment with mCGP for 48 h, proving that mCGP could indeed catalyze the breakdown of the abundant H₂O₂ in cancers to mitigate the cancer hypoxia environment. Similarly, the excellent anticancer efficiency of mCGP was also confirmed by weighting (Figure 6D) and photographing (Figure 6E) the corresponding sacrificed cancers. The cancer inhibition ratios reached about 67.5%, 80.9%, 90.9%, 54.4% and 97.1% after treatment with PCN-224 and light, mCP and light, mGP and light, mCGP in the absence or presence of light, respectively. Consistent with previous results, after treatment with mCGP and light, obvious cancer cells damages were detected by hematoxylin and eosin (H&E) staining (Figure 6G). Above results strongly confirmed the superior anticancer efficacy of mCGP. Also, the body weights of the mice had no obvious changes during the 14 days treatment (Figure 6C). And no obvious changes were observed in the hematological parameters (Figure S25) and blood biochemical levels of the mice after treatment with mCGP for 14 days (Figure S26). No hemolysis of red blood cells was detected after treatment with various amounts of mCGP (Figure S27). These results confirmed that mCGP had a good biocompatibility for biological applications. Moreover, no significantly

physiological morphology changes were found in the main organs including heart, liver, spleen, lung and kidney by H&E staining (Figure S28), indicating no obviously systemic toxicity of mCGP during the treatment. To further explore the excretion of mCGP *in vivo*, the fate of Zr element from excrement was measured after treatment with mCGP for various times using ICP-MS. As illustrated in Figure S29, high levels of Zr were detected in the urine and feces of mice, confirming that mCGP could be efficiently excreted out of body and it was beneficial to the biomedicine application.

CONCLUSIONS

In conclusion, an intelligent cascade bioreactor of mCGP was constructed to enhance the anticancer efficiency by starvation therapy and PDT. Due to its biomimetic surface functionalization, mCGP could evade the immune clearance and exhibit homotypic targeting behavior, which would extensively improve its cancer accumulation and retention ability. After internalized by cancer cells, the cascade reactions of mCGP would simultaneously cut off the cancer cell glucose metabolism and destroy the intracellular elements by PDT. Moreover, by converting H_2O_2 to O_2 , mCGP was suitable for spatiotemporally controlled cancer treatment by mitigating the cancer hypoxia. Subsequently, the long-term cancer starvation therapy and robust PDT of mCGP would efficiently inhibit the cancer growth after a single treatment with no obvious side effects. This cascade bioreactor would further promote the development of complementary modes for more effective cancer treatment in spite of the unfavorable cancer microenvironment

MATERIALS AND METHODS

Materials and Methods. Methanol, dichloromethane (DCM), dimethyl sulphoxide (DMSO) and N, N'-dimethylformamide (DMF) were obtained from Shanghai Chemical Co. (China)., 2', 7'-dichlorofluorescein diacetate (DCFH-DA) was obtained from R&D-SYSTEMS. Singlet oxygen sensor green (SOSG), Annexin V-FITC, Propidium Iodide (PI), Dulbecco's phosphate buffered saline (PBS), trypsin, Dulbecco's modified Eagle's medium (DMEM), RPMI 1640 and 3-[4,5-dimethylthiazol-2-yl]-2,5-diphenyltetrazolium-bromide (MTT), Hoechst 33342, fetal bovine serum (FBS), penicillin-streptomycin, LysoTracker Green and MitoTracker Green were purchased from Invitrogen Corp.. NaN₃, Glucose, glucose oxidase (GOx) and catalase were purchased from Sigma Aldrich Corp.. The BCA reagents and the Membrane Protein Extraction Kit were purchased from Beyotime. All other reagents were of analytical grade and used as received. Fluorescence spectrum was measured on a LS55 luminescence spectrometer (Perkin-Elmer). The excitation wavelength for SOSG was 494 nm, and its emission wavelength was collected at 504 nm. The particle size and zeta potential was measured by Nano-ZS ZEN3600 (Malvern Instruments). TGA was measured by Pyris1 thermo gravimetric analyzer (Perkin-Elmer). SEM images were obtained by using scanning electron microscope (Sigma). TEM images were obtained by Tecnai G20 S-TWIN. PXRD was measured by Rigaku MiniFlex. The dissolved oxygen was measured by Dissolved oxygen meter (Leici Corp., PHSJ-3F). The *in vitro* photodynamic therapy was conducted using 660 nm LED (light emitting diode) light (29.8 mW cm⁻²). The *in vivo* experiments were irradiated using 660 nm He-Ne laser (150 mW cm⁻²). The *in vivo* imaging experiments were carried out using IVIS imaging systems (Perkin-Elmer), and the excitation wavelength was used at 640 nm, its emission wavelength was collected around 700 nm. The cell viability was measured using microplate reader (Bio-Rad, Model 550, USA). The polycarbonate porous membrane (400 nm) and Avanti mini extruder were obtained from Avanti Polar Lipids. Fluorescence microscopy images were observed using a confocal laser scanning

microscopy (CLSM, C1-Si, Nikon, Japan). Fluorescence spectrum were taken using L55 fluorescence microscopy (Perkin-Elmer). Flow cytometry (BD FACSAria TM III) was used to analysis the cellular uptake behaviors and cell death analysis. The UV-vis absorbance was measured by UV-vis spectroscopy (Lambda Bio40). Blood biochemistry and blood routine were analyzed by Blood Biochemistry Analyzer (MNCHIP POINTCARE) and Auto Hematology Analyzer (MC-6200VET).

Synthesis of PCN-224. PCN-224 was synthesized according to the reported literature. Briefly, TCPP (100 mg), $\text{ZrOCl}_2 \cdot 8\text{H}_2\text{O}$ (300 mg) and benzoic acid (2.8 g) were dissolved in DMF (100 mL) and stirred for 5 h at 90 °C. After which, the obtained mixture was centrifuged at (12000 rpm) for 30 min. The obtained particles were thoroughly washed by DMF for 3 times. The obtained PCN-224 particles were stored in DMF solution in the shield of light.

The Preparation of Cell Membrane Fragments. The murine mammary carcinoma (4T1) cell membrane was obtained using Membrane Protein Extraction Kit. Briefly, the collected cells were dispersed in membrane protein extraction buffer solutions and cooled in an ice bath for 10-15 min. After which, the cells were freezing-thawing for 3 cycles. And then, the obtained mixture was centrifuged (700 g, 10 min, 4 °C) and the supernatant was further centrifuged (14,000 g, 30 min). Finally, the 4T1 cell membrane was obtained by lyophilizing the precipitate.

The Preparation of mCP, mGP and mCGP. The mCP, mGP and mCGP was prepared using Avanti mini extruder. Briefly, the pre-prepared PCN-224 was thoroughly washed with distilled water for several times and then dispersed in distilled water. The solid 4T1 cell membrane solids were dissolved in distilled water. A certain amount of GOx and catalase was added into 0.5 mL of PCN-224 (2 mg/mL). And then, 0.5 mL of 4T1 cell membrane (2 mg/mL) was added into the mixture. Finally, the mixture was extruded by Avanti mini extruder using polycarbonate porous

membrane (400 nm). mCP, mGP and mCGP were obtained by centrifugation and they were quantitatively measured using UV-Vis spectroscopy (at 518 nm). For the *in vitro* experiments, 10 μ g of GOx and 380 U of catalase were added to prepare mCGP. For the *in vivo* experiments, 250 μ g of GOx and 2280 U of catalase was added to prepare the mCGP. The obtained materials were further characterized by the other instruments.

Cell Cultures. African green monkey fibroblast (COS7) cells and murine macrophages (RAW264.7) cells were incubated in DMEM medium containing 10% FBS and 1% antibiotics (penicillin-streptomycin, 10 000 U/mL). 4T1 cells were incubated in RPMI1640 medium containing 10% FBS and 1% antibiotics (penicillin-streptomycin, 10 000 U/mL). The cell experiments were conducted in glucose-free RPMI1640 medium. To mimic the normoxia environment, the cells were cultured at 37 °C in a humidified atmosphere containing 21% O₂ and 5% CO₂. To mimic the hypoxia environment, the cells were cultured at 37 °C in a humidified atmosphere containing 2% O₂ and 5% CO₂.

The Catalytic Activity Measurements of mCGP. Firstly, mCGP induced pH change was measured in the absence or presence of glucose. Briefly, mCGP (50 μ g/mL) was mixed with glucose (1 mg/mL) or dispersed in distilled water alone. The real time pH values of the solutions were measured by pH meter. Also, the dissolved O₂ in mCGP (50 μ g/mL) solutions were also measured in the absence or presence of glucose (1 mg/mL) and in the absence or presence of H₂O₂ (10 mM) using dissolved oxygen meter.

The ¹O₂ Production Ability of mCGP. Firstly, the OFF/ON irradiation response of ¹O₂ production was evaluated. mCGP (50 μ g/mL) was dispersed in distilled water. After which, SOSG (5 μ M) was added in the shield of light. And then, the solution was irradiated (660 nm He-

Ne laser, 150 mW/cm²) or stored in the shield of light. The fluorescence of the solution was measured at the time intervals.

Then, the effects of H₂O₂, N₂ and NaN₃ on ¹O₂ production were also evaluated. mCGP (50 µg/mL) and SOSG (5 µM) was added in the presence or absence of NaN₃ (1 mM). And then, the solution was irradiated at the time intervals or stored in the shield of light. The fluorescence of the solution was monitored using fluorescence spectroscopy. To mimic the hypoxia environment, mCGP (50 µg/mL) solution was purged with N₂ for 1 h. After which, SOSG (5 µM) was added. And then, the solution was irradiated or stored in the shield of light in the presence or absence of H₂O₂ (1 mM).

Besides, the ROS production in living cells was also assessment. 4T1 cells were seeded in Petri dishes and incubated for 24 h. mCGP (40 µg/mL), PCN-224 (40 µg/mL) or TCPP (40 µg/mL) in glucose-free RPMI1640 medium was added and incubated with the cells for 6 h. And then, the cells were washed by PBS and incubated with DCFH-DA (5 µM) for 30 min. After which, the cells were incubated in the shield of light or irradiated for 5 min (660 nm LED light, 29.8 mW/cm²). The cells were then observed by CLSM. Moreover, the ROS production ability of mCGP was also measured using flow cytometry. After treatment for 6 h using the similar method, the cells were digested by trypsin, collected by centrifugation (1500 r/min), washed with PBS and analyzed by flow cytometry.

Cellular Uptake Behaviors of mCGP. COS7 cells, 4T1 cells, B16F10 cells and HepG2 cells were seeded and incubated for 24 h, respectively. After which, mCGP (40 µg/mL) was added and incubated with the cells for 3 h. And then, the cells were washed by PBS for 3 times, stained by Hoechst 33342 for 15 min and observed by CLSM. Furthermore, the cellular uptake of mCGP was also measured by flow cytometry. After incubation with mCGP (40 µg/mL) for 3 h, the cells

were collected and analyzed by flow cytometry. Moreover, the cellular uptake behaviors of PCN-224 and mCGP against RAW264.7 cells were also evaluated using CLSM and flow cytometry. Briefly, RAW264.7 cells were incubated with PCN-224 (40 $\mu\text{g/mL}$) or mCGP (40 $\mu\text{g/mL}$) for 3 h. The cells were washed by PBS and observed by CLSM and analyzed by flow cytometry.

Subcellular Locations of mCGP. 4T1 cells were seeded and incubated for 24 h. And then, mCGP (40 $\mu\text{g/mL}$) was added and incubated with the cells for 3 h. Then, the cells were washed by PBS for 3 times and stained with MitoTracker Green (500 nM) or LysoTracker Green (500 nM) for 30 min, respectively. Finally, the cells were washed by PBS, observed and analyzed by CLSM.

Cytotoxicity Measurements. The cytotoxicity was measured by MTT Assay. 4T1 cells and COS7 cells were cultured on 96-well plates. After 24 h, gradient concentrations of mGP, mCP or mCGP were added into each well. After incubation for 4 h in the normoxia (21% O_2) or hypoxia (2% O_2) environment, mGP, mCP or mCGP contained culture medium was extracted and fresh glucose-free RPMI1640 medium (100 μL) was added to each well. Subsequently, the cells were irradiated for 5 min (660 nm LED light, 29.8 mW/cm^2) or incubated in the shield of light. After further incubation for 24 h, MTT (20 μL , 5 mg/mL) was added into each well. And then, the MTT contained culture medium was replaced with 150 μL of DMSO after incubation for 4 h. The absorbance was measured using Microplate reader (BIO-RAD 550). The cell viabilities (%) were calculated as follows: $100 \times \text{OD}_{(\text{samples})}/\text{OD}_{(\text{control})}$, where $\text{OD}_{(\text{control})}$ and $\text{OD}_{(\text{samples})}$ represented the absorbance in the absence and presence of samples at 570 nm. To evaluate the influence of light irradiation, the cell viabilities of 4T1 and COS7 cells without any treatment were measured in the absence and presence of light using the same method.

Moreover, the cytotoxicity was also evaluated by flow cytometry. After incubation with mGP (40 µg/mL), mCP (40 µg/mL) or mCGP (40 µg/mL) for 4 h or without any treatment, the cells were irradiated for 5 min or incubated in the shield of light. After which, the cells were incubated in the shield of light for 24 h. And then, the cells were harvested and stained by Annexin V-FITC/PI and analyzed by flow cytometry.

In Vivo Imaging. All of the animal experiments were conducted with the approval of the Institutional Animal Care and Use Committee of the Animal Experiment Center of Wuhan University (Wuhan, China) as well as the Regulations for the Administration of Affairs Concerning Experimental Animals. 4T1 cancer bearing Balb/c mice were intravenously injected with PCN-224 (200 µL, 1 mg/mL) or mCGP (200 µL, 1 mg/mL), respectively. After which, the fluorescence were observed using IVIS imaging systems at 30 min, 12 h, 24 h, 36 h, 48 h, 60 h, 72 h, 84 h and 96 h. Moreover, the cancer tissues in parallel groups were sacrificed after injection of PCN-224 or mCGP for 24 h, 48 h, 72 h and 96 h. The sacrificed cancer tissues and the collected organs were observed and analyzed by IVIS imaging systems.

Anticancer Studies. 4T1 cancer bearing Balb/c mice (seven to eight weeks) were randomized divided into 9 groups (5 mice in each group). When the cancer volume reached about 100 mm³, the mice were intravenously injected with PBS, PCN-224 (200 µL, 1 mg/mL), mGP (200 µL, 1 mg/mL), mCP (200 µL, 1 mg/mL) or mCGP (200 µL, 1 mg/mL). After 48 h, the mice were irradiated with He-Ne laser (660 nm, 150 mW/cm²) or without any treatment. The cancer volume and the body weight were recorded every other day. The cancer volume was calculated as follows: $V = W^2 \times L/2$, where W and L represented the length in minor and major. The relative cancer volume and relative body weight were corresponding changes compared with the first day. After 14 days, the cancer tissues and the main organs were sacrificed for histological analysis.

Hemolysis Test. Blood cells were collected from BALB/c mice and incubated with different amounts of mCGP in tubes at 37 °C. After 30 min, the samples were centrifuged to examine the hemolysis. The blood cells in PBS and the blood cells in distilled water without adding mCGP were used as controls.

Blood Biochemistry and Blood Routine Examination. BALB/c mice were intravenously injected with mCGP (200 µL, 1 mg/mL). After 14 days, the blood was collected and then analyzed by Blood Biochemistry Analyzer (MNCHIP POINTCARE) and Auto Hematology Analyzer (MC-6200VET).

Excretion Study. The excrement of the mice was collected to investigate the excretion of mCGP. Briefly, the mice were intravenously injected with mCGP and housed in metabolic cages. The collected urine and feces was digested by chloroazotic acid and analyzed by ICP-MS.

ASSOCIATED CONTENT

Supporting Information. Standard curve of BSA, TGA analysis of PCN-224 and CGP, hydrodynamic size distribution of mCGP, zeta potential changes of mCGP in 7 days, western blot analysis of protein markers' expression in 4T1 cell membrane, mCGP and 4T1 cells, PXRD patterns of CGP, mCP and mGP, pH changes of GOx and glucose solutions in the presence or absence of O₂, O₂ concentration changes in the solutions of glucose, GOx or glucose and GOx, glucose concentration related pH changes after treatment with GO_x, GOx concentration related pH changes after treatment with glucose, O₂ concentration changes in the solutions of H₂O₂, catalase, H₂O₂ and catalase, macroscopic images of the solutions in the presence of H₂O₂, mCGP and H₂O₂, or mCGP, CLSM images of 4T1 cells after treatment with TCPP and DCFH-DA after irradiation, CLSM images of B16F10 cells and HepG2 cells after treatment with mCGP, UV-Vis absorbance spectrum of mCGP, cell viabilities of glucose, GOx, H₂O₂, PCN-224, catalase and mCP against 4T1 cells, cell viabilities of 4T1 cells and COS7 cells with or without irradiation, representative photos of the cancer size of the mice after various treatments for 1 day, 7 days and 14 days, hematological parameters and blood biochemical parameters of the mice after treatment with mCGP, hemolysis analysis, the ICP-MS analysis of Zr element in the urine and feces. This material is available free of charge *via* the Internet at <http://pubs.acs.org>.

AUTHOR INFORMATION

Corresponding Author

*Corresponding Author: xz-zhang@whu.edu.cn

ORCID

Xian-Zheng Zhang: 0000-0001-6242-6005

Notes

The authors declare no competing financial interest.

ACKNOWLEDGMENT

This work was supported by the National Natural Science Foundation of China (51233003, 51533006 and 51690152).

REFERENCES

1. Vander Heiden, M. G. Targeting Cancer Metabolism: a Therapeutic Window Opens. *Nat. Rev. Drug Discov.* **2011**, *10*, 671-684.
2. Schulze, A.; Harris, A. L. How Cancer Metabolism is Tuned for Proliferation and Vulnerable to Disruption. *Nature* **2012**, *491*, 364-373.
3. Cheong, H.; Lu, C.; Lindsten, T.; Thompson, C. B. Therapeutic Targets in Cancer Cell Metabolism and Autophagy. *Nat. Biotechnol.* **2012**, *30*, 671-678
4. Galluzzi, L.; Kepp, O.; Vander Heiden, M. G.; Kroemer, G. Metabolic Targets for Cancer Therapy. *Nat. Rev. Drug Discov.* **2013**, *12*, 829-846.
5. Kroemer, G.; Pouyssegur, J. Tumor Cell Metabolism: Cancer's Achilles' Heel. *Cancer cell* **2008**, *13*, 472-482.
6. Tennant, D. A.; Durán, R. V.; Gottlieb, E. Targeting Metabolic Transformation for Cancer Therapy. *Nat. Rev. Cancer* **2010**, *10*, 267-277.
7. Cairns, R. A.; Harris, I. S.; Mak, T. W. Regulation of Cancer Cell Metabolism. *Nat. Rev. Cancer* **2011**, *11*, 85-95.
8. Denko, N. C. Hypoxia, HIF1 and Glucose Metabolism in the Solid Tumour. *Nat. Rev. Cancer* **2008**, *8*, 705-713
9. Koppenol, W. H.; Bounds, P. L.; Dang, C. V. Otto Warburg's Contributions to Current Concepts of Cancer Metabolism. *Nat. Rev. Cancer* **2011**, *11*, 325-337.
10. Vander Heiden, M. G.; Cantley, L. C.; Thompson, C. B. Understanding the Warburg effect: the Metabolic Requirements of Cell Proliferation. *Science* **2009**, *324*, 1029-1033.
11. Gatenby, R. A.; Gillies, R. J. Why do Cancers Have High Aerobic Glycolysis? *Nat. Rev. Cancer* **2004**, *4*, 891-899.

12. Izuishi, K.; Kato, K.; Ogura, T.; Kinoshita, T.; Esumi, H. Remarkable Tolerance of Tumor Cells to Nutrient Deprivation: Possible New Biochemical Target for Cancer Therapy. *Cancer Res.* **2000**, *60*, 6201-6207.
13. Fan, W.; Lu, N.; Huang, P.; Liu, Y.; Yang, Z.; Wang, S.; Yu, G. C.; Liu, Y. J.; Hu, J. K.; He, Q. J.; Qu, J. L.; Wang, T. F.; Chen, X. Y. Glucose-Responsive Sequential Generation of Hydrogen Peroxide and Nitric Oxide for Synergistic Cancer Starving-Like/Gas Therapy. *Angew. Chem. Int. Ed.* **2017**, *56*, 1229-1233.
14. Kim, J.; Dang, C. V. Cancer's Molecular Sweet Tooth and the Warburg Effect. *Cancer Res.* **2006**, *66*, 8927-8930.
15. Zhang, C.; Ni, D.; Liu, Y. Y.; Yao, H. L.; Bu, W. B.; Shi, J. L. Magnesium Silicide Nanoparticles as a Deoxygenation Agent for Cancer Starvation Therapy. *Nat. Nanotechnol.* **2017**, doi:10.1038/nnano.2016.280;
16. Brannon-Peppas, L.; Blanchette, J. O. Nanoparticle and Targeted Systems for Cancer Therapy. *Adv. Drug Deliv. Rev.* **2012**, *64*, 206-212.
17. Kim, S. M.; Roy, S. G.; Chen, B.; Nguyen, T. M.; McMonigle, R. J.; McCracker, A. N.; Zhang, Y. L.; Kofuji, S.; Hou, J.; Selwan, E.; Finicle, B. T.; Nguyen, T. T.; Ravi, A.; Ramirez, M. U.; Wiher, T.; Guenther, G. G.; Kono, M.; Edwards, A. T.; Hanessian, S.; Edinger, A. L. Targeting Cancer Metabolism by Simultaneously Disrupting Parallel Nutrient Access Pathways. *J. Clin. Invest.* **2016**, *126*, 4088-4102.
18. Selwan, E. M.; Finicle, B. T.; Kim, S. M.; Edinger, A. L. Attacking the Supply Wagons to Starve Cancer Cells to Death. *FEBS Lett.* **2016**, *590*, 885-907.
19. Zhao, Y.; Butler, E. B.; Tan, M. Targeting Cellular Metabolism to Improve Cancer Therapeutics. *Cell Death Dis.* **2013**, *4*, e532.

20. Liu, Y.; Zhang, W. H.; Cao, Y. Y.; Liu, Y.; Bergmeier, S.; Chen, X. Z. Small Compound Inhibitors of Basal Glucose Transport Inhibit Cell Proliferation and Induce Apoptosis in Cancer Cells Via Glucose-Deprivation-Like Mechanisms. *Cancer Lett.* **2010**, *298*, 176-185.
21. Ochsner, M. Photophysical and Photobiological Processes in the Photodynamic Therapy of Tumours. *J. Photochem. Photobiol. B-Biol.* **1997**, *39*, 1-18.
22. Dolmans, D. E.; Fukumura, D.; Jain, R. K. Photodynamic Therapy for Cancer. *Nat. Rev. Cancer* **2003**, *3*, 380-387.
23. Brown, S. B.; Brown, E. A.; Walker, I. The Present and Future Role of Photodynamic Therapy in Cancer Treatment. *Lancet Oncol.* **2004**, *5*, 497-508.
24. Secret, E.; Maynadier, M.; Gallud, A.; Chaix, A.; Bouffard, E.; Gary-Bobo, M.; Marcotte, N.; Mongin, O.; Cheikh, K. E.; Hugues, V.; Auffan, M.; Frochot, C.; Morère, A.; Maillard, P.; Blanchard-Desce, M.; Sailor, M. J.; Garcia, M.; Durand, J.-O.; Cunin, F. Two-Photon Excitation of Functionalized Porous Silicon Nanoparticles for Photodynamic Therapy. *Adv. Mater.* **2014**, *26*, 7643-7648.
25. Abbas, M.; Zou, Q. L.; Li, S. K.; Yan, X. H. Self-Assembled Peptide- and Protein-Based Nanomaterials for Antitumor Photodynamic and Photothermal Therapy. *Adv. Mater.* **2017**, doi: 10.1002/adma.201605021.
26. Huang, P.; Lin, J.; Wang, X. S.; Wang, Z.; Zhang, C. L.; He, M.; Wang, K.; Chen, F.; Li, Z. M.; Shen, G. X.; Cui, D. X.; Chen, X. Y. Light-Triggered Theranostics Based on Photosensitizer-Conjugated Carbon Dots for Simultaneous Enhanced-Fluorescence Imaging and Photodynamic Therapy. *Adv. Mater.* **2012**, *24*, 5104-5110.
27. Qian, C. G.; Feng, P. J.; Yu, J. C.; Chen, Y. L.; Hu, Q. Y.; Sun, W. J.; Xiao, X. Z.; Hu, X. L.; Bellotti, A.; Shen, Q. D.; Gu, Z. Anaerobe-Inspired Anticancer Nanovesicles. *Angew. Chem. Int. Ed.* **2017**, *56*, 2588-2593.

28. Wang, C.; Sun, X. Q.; Cheng, L.; Yin, S. N.; Yang, G. B.; Li, Y. G.; Liu, Z. Multifunctional Theranostic Red Blood Cells For Magnetic-Field-Enhanced *In Vivo* Combination Therapy of Cancer. *Adv. Mater.* **2014**, *26*, 4794-4802.
29. Chatterjee, D. K.; Fong, L. S.; Zhang, Y. Nanoparticles in Photodynamic Therapy: An Emerging Paradigm. *Adv. Drug Deliv. Rev.* **2008**, *60*, 1627-1637.
30. Lin, J.; Wang, S. J.; Huang, P.; Wang, Z.; Chen, S. H.; Niu, G.; Li, W. W.; He, J.; Cui, D. X.; Lu, G. M.; Chen, X. Y.; Nie, Z. H. Photosensitizer-Loaded Gold Vesicles with Strong Plasmonic Coupling Effect for Imaging-Guided Photothermal/Photodynamic Therapy. *ACS Nano* **2013**, *7*, 5320-5329.
31. Kievit, F. M.; Zhang, M. Cancer Nanotheranostics: Improving Imaging and Therapy by Targeted dDelivery Across Biological Barriers. *Adv. Mater.* **2011**, *23*, H217-H247.
32. Lu, K. D.; He, C. B.; Guo, N. N.; Chan, C.; Ni, K. Y.; Weichselbaum, R. R.; Lin, W. B. Chlorin-Based Nanoscale Metal-Organic Framework Systemically Rejects Colorectal Cancers via Synergistic Photodynamic Therapy and Checkpoint Blockade Immunotherapy. *J. Am. Chem. Soc.* **2016**, *138*, 12502-12510.
32. Lu, K. D.; He, C. B.; Lin, W. B. Nanoscale Metal-Organic Framework for Highly Effective Photodynamic Therapy of Resistant Head and Neck Cancer. *J. Am. Chem. Soc.* **2014**, *136*, 16712-16715.
33. Lu, K. D.; He, C. B.; Lin, W. B. A Chlorin-Based Nanoscale Metal-Organic Framework for Photodynamic Therapy of Clon Cancers. *J. Am. Chem. Soc.* **2015**, *137*, 7600-7603.
34. Park, J.; Jiang, Q.; Feng, D. W.; Mao, L. Q.; Zhou, H. C. Size-Controlled Synthesis of Porphyrinic Metal-Organic Framework and Functionalization for Targeted Photodynamic Therapy. *J. Am. Chem. Soc.* **2016**, *138*, 3518-3525.

35. Liu, J. J.; Yang, Y.; Zhu, W. W.; Yi, X.; Dong, Z. L.; Xu, X. N.; Chen, M. W.; Yang, K.; Lu, G.; Jiang, L. X.; Liu, Z. Nanoscale Metal-Organic Frameworks for Combined Photodynamic & Radiation Therapy in Cancer Treatment. *Biomaterials* **2016**, *97*, 1-9.
36. Lismont, M.; Dreesen, L.; Wuttke, S. Metal-Organic Framework Nanoparticles in Photodynamic Therapy: Current Status and Perspectives. *Adv. Funct. Mater.* **2017**, doi: 10.1002/adfm.201606314.
37. Qian, C. G.; Yu, J. C.; Chen, Y. L.; Hu, Q. Y.; Xiao, X. Z.; Sun, W. J.; Wang, C.; Feng, P. J.; Shen, Q. D.; Gu, Z. Light-Activated Hypoxia-Responsive Nanocarriers for Enhanced Anticancer Therapy. *Adv. Mater.* **2016**, *28*, 3313-3320.
38. Chen, H. C.; Tian, J. W.; He, W. J.; Guo, Z. J. H₂O₂-Activatable and O₂-Evolving Nanoparticles for Highly Efficient and Selective Photodynamic Therapy Against Hypoxic Tumor Cells. *J. Am. Chem. Soc.* **2015**, *137*, 1539-1547.
39. Zhu, W. W.; Dong, Z. L.; Fu, T. T.; Liu, J. J.; Chen, Q.; Li, Y. G.; Zhu, R.; Xu, L. G.; Liu, Z. Modulation of Hypoxia in Solid Tumor Microenvironment with MnO₂ Nanoparticles to Enhance Photodynamic Therapy. *Adv. Funct. Mater.* **2016**, *26*, 5490-5498.
40. Chen, Q.; Feng, L. Z.; Liu, J. J.; Zhu, W. W.; Dong, Z. L.; Wu, Y. F.; Liu, Z. Intelligent Albumin-MnO₂ Nanoparticles as pH-/H₂O₂-Responsive Dissociable Nanocarriers to Modulate Tumor Hypoxia for Effective Combination Therapy. *Adv. Mater.* **2016**, *28*, 7129-7136.
41. Fan, W. P.; Bu, W. B.; Shen, B.; He, Q. J.; Cui, Z. W.; Liu, Y. Y.; Zheng, X. P.; Zhao, K. L.; Shi, J. L. Intelligent MnO₂ Nanosheets Anchored with Upconversion Nanoprobes for Concurrent pH-/H₂O₂-Responsive UCL Imaging and Oxygen-Elevated Synergetic Therapy. *Adv. Mater.* **2015**, *27*, 4155-4161.

42. Knop, K.; Hoogenboom, R.; Fischer, D.; Schubert, U. S. Poly (ethylene glycol) in Drug Delivery: Pros and Cons as well as Potential Alternatives. *Angew. Chem. Int. Ed.* **2010**, *49*, 6288-6308.
43. Li, Y. T.; Tang, J. L.; He, L. C.; Liu, Y.; Liu, Y. L.; Chen, C. Y.; Tang, Z. Y. Core-Shell Upconversion Nanoparticle@ Metal-Organic Framework Nanoprobes for Luminescent/Magnetic Dual-Mode Targeted Imaging. *Adv. Mater.* **2015**, *27*, 4075-4080.
44. Li, S. D.; Huang, L. Stealth Nanoparticles: High Density but Sheddable PEG is a Key for Tumor Targeting. *J. Control. Release* **2010**, *145*, 178-181.
45. Rao, L.; Bu, L. L.; Cai, B.; Xu, J. H.; Li, A.; Zhang, W. F.; Sun, Z. J.; Guo, S. S.; Liu, W.; Wang, T. H.; Zhao, X. Z. Cancer Cell Membrane-Coated Upconversion Nanoprobes for Highly Specific Tumor Imaging. *Adv. Mater.* **2016**, *28*, 3460-3466.
46. Ishida, T.; Ichihara, M.; Wang, X. Y.; Yamanoto, K.; Kimura, J.; Majima, E.; Kiwada, H. Injection of PEGylated Liposomes in Rats Elicits PEG-Specific IgM, which is Responsible for Rapid Elimination of a Second Dose of PEGylated Liposomes. *J. Control. Release* **2006**, *112*, 15-25.
47. Wang, X. Y.; Ishida, T.; Kiwada, H. Anti-PEG IgM Elicited by Injection of Liposomes is Involved in the Enhanced Blood Clearance of a Subsequent Dose of PEGylated Liposomes. *J. Control. Release* **2007**, *119*, 236-244.
48. Fang, R. H.; Hu, C. M. J.; Luk, B. T.; Gao, W. W.; Copp, J. A.; Tai, Y. Y.; O'Connor, D. E.; Zhang, L. F. Cancer Cell Membrane-Coated Nanoparticles for Anticancer Vaccination and Drug Delivery. *Nano Lett.* **2014**, *14*, 2181-2188.
49. Zou, W. Immunosuppressive Networks in the Tumour Environment and Their Therapeutic Relevance. *Nat. Rev. Cancer* **2005**, *5*, 263-274.

50. Rodriguez, P. L.; Harada, T.; Christian, D. A.; Pantano, D. A.; Tsai, R. K.; Discher, D. E. Minimal "Self" Peptides that Inhibit Phagocytic Clearance and Enhance Delivery of Nanoparticles. *Science* **2013**, *339*, 971-975.
51. Rao, L.; Cai, B.; Bu, L. L.; Liao, Q. Q.; Guo, S. S.; Zhao, X. Z.; Dong, W. F.; Liu, W. Microfluidic Electroporation-Facilitated Synthesis of Erythrocyte Membrane-Coated Magnetic Nanoparticles for Enhanced Imaging-Guided Cancer Therapy. *ACS Nano* **2017**, doi: 10.1021/acsnano.7b00133.
52. Cheng, H.; Zhu, J. Y.; Li, S. Y.; Zeng, J. Y.; Lei, Q.; Chen, K. W.; Zhang, C.; Zhang, X. Z. An O₂ Self-Sufficient Biomimetic Nanoplatform for Highly Specific and Efficient Photodynamic Therapy. *Adv. Funct. Mater.* **2016**, *26*, 7847-7680.
53. Chen, W. S.; Zeng, K.; Liu, H.; Ouyang, J.; Wang, L. Q.; Liu, Y.; Wang, H.; Deng, L.; Liu, Y. N. Cell Membrane Camouflaged Hollow Prussian Blue Nanoparticles for Synergistic Photothermal-/Chemotherapy of Cancer. *Adv. Funct. Mater.* **2017**, doi: 10.1002/adfm.201605795.
54. Zhu, J. Y.; Zheng, D. W.; Zhang, M. K.; Yu, W. Y.; Qiu, W. X.; Hu, J. J.; Feng, J.; Zhang, X. Z. Preferential Cancer Cell Self-Recognition and Tumor Self-Targeting by Coating Nanoparticles with Homotypic Cancer Cell Membranes. *Nano Lett.* **2016**, *16*, 5895-5901.
55. Tang, J.; Shen, D.; Caranasos, T. G.; Wang, Z.; Vandergriff, A. C.; Allen, T. A.; Hensley, M. T.; Dinh, P.; Cores, J. U.; Li, T. S.; Zhang, J. Y.; Kan, Q. C.; Cheng, K. Therapeutic Microparticles Functionalized with Biomimetic Cardiac Stem Cell Membranes and Secretome. *Nat. Commun.* **2017**, *8*, 13724.
56. Sun, H. P.; Su, J. H.; Meng, Q. S.; Yin, Q.; Chen, L. L.; Gu, W. W.; Zhang, P. C.; Zhang, Z. C.; Zhang, Z. W.; Yu, H. J.; Wang, S. L.; Li, Y. P. Cancer-Cell-Biomimetic Nanoparticles for Targeted Therapy of Homotypic Tumors. *Adv. Mater.* **2016**, *28*, 9581-9588.

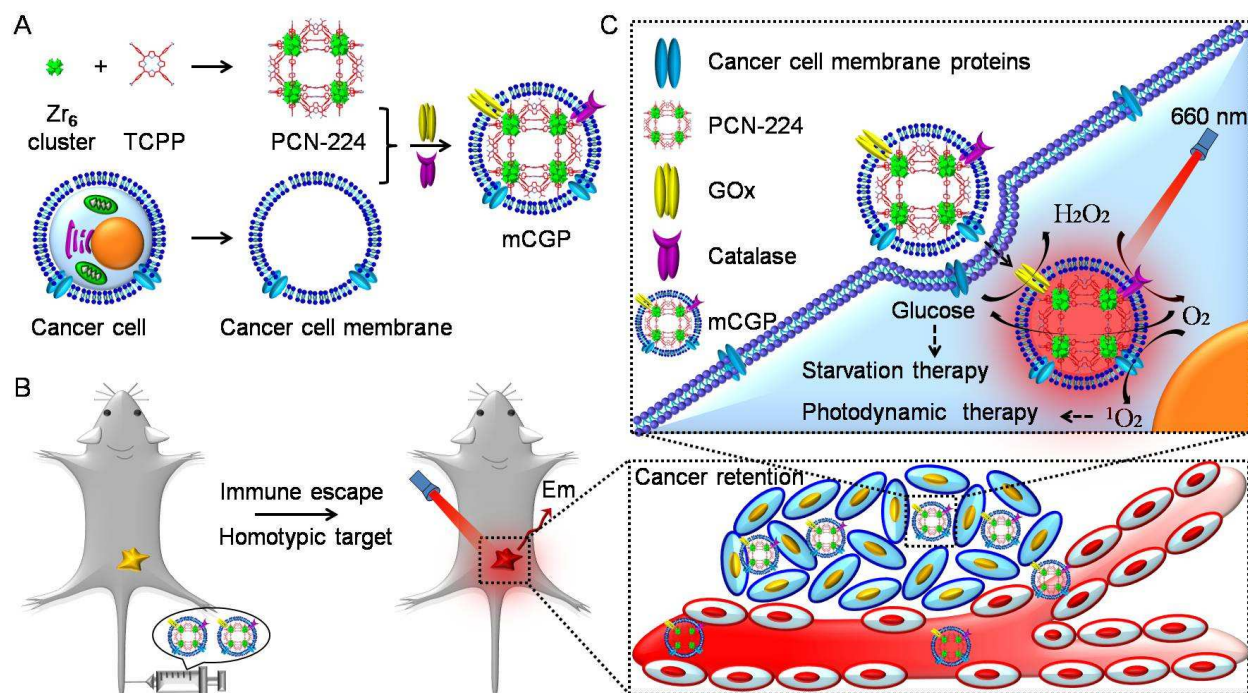
57. Gao, W. W.; Hu, C. M. J.; Fang, R. H.; Luk, B. T.; Su, J.; Zhang, L. F. Surface Functionalization of Gold Nanoparticles with Red Blood Cell Membranes. *Adv. Mater.* **2013**, *25*, 3549-3553.
58. Hu, Q. Y.; Sun, W. J.; Qian, C. G.; Wang, C.; Bomba, H. N.; Gu, Z. Anticancer Platelet-Mimicking Nanovehicles. *Adv. Mater.* **2015**, *27*, 7043-7050.
59. Copp, J. A.; Fang, R. H.; Luk, B. T.; Hu, C. M. J.; Gao, W. W.; Zhang, K.; Zhang, L. F. Clearance of Pathological Antibodies Using Biomimetic Nanoparticles. *Proc. Natl. Acad. Sci. U. S. A.* **2014**, *111*, 13481-13486.
60. Tan, S.; Wu, T.; Zhang, D.; Zhang, Z. P. Cell or Cell Membrane-Based Drug Delivery Systems. *Theranostics* **2015**, *5*, 863-881.
61. Dehaini, D.; Wei, X.; Fang, R. H.; Masson, S.; Angsantikul, P.; Luk, B. T.; Zhang, Y.; Ying, M.; Jiang, Y.; Kroll, A. V.; Gao, W. W.; Zhang, L. F. Erythrocyte-Platelet Hybrid Membrane Coating for Enhanced Nanoparticle Functionalization. *Adv. Mater.* **2017**, doi: 10.1002/adma.201606209.
62. Hu, C. M. J.; Fang, R. H.; Wang, K. C.; Luk, B. T.; Thamphiwatana, S.; Dehaini, D.; Nguyen, P.; Angsantikul, P.; Wen, C. H.; Kroll, A. V.; Carpenter, C.; Ramesh, M.; Qu, V.; Patel, S. H.; Zhu, J.; Shi, W.; Hofman, F. M.; Chen, T. C.; Gao, W. W.; Zhang, K.; Chien, S.; Zhang, L. F. Nanoparticle Biointerfacing by Platelet Membrane Cloaking. *Nature* **2015**, *526*, 118-121.
63. Cao, H. Q.; Dan, Z. L.; He, X. Y.; Zhang, Z. W.; Yu, H. J.; Yin, Q.; Li, Y. P. Liposomes Coated with Isolated RAW264.7 Membrane Can Target Lung Metastasis of Breast Cancer. *ACS Nano* **2016**, *10*, 7738-7748.
64. Sun, H. P.; Su, J. H.; Meng, Q. H.; Yin, Q.; Chen, L. L.; Gu, W. W.; Zhang, Z. W.; Yu, H. J.; Zhang, P. C.; Wang, S. L.; Li, Y. P. Cancer Cell Membrane-Coated Gold Nanocages with

- Hyperthermia - Triggered Drug Release and Homotypic Target Inhibit Growth and Metastasis of Breast Cancer. *Adv. Funct. Mater.* **2017**, 27, doi: 10.1002/adfm.201604300.
65. Hu, C. M. J.; Fang, R. H.; Luk, B. T.; Zhang, L. F. Nanoparticle-Detained Toxins for Safe and Effective Vaccination. *Nature Nanotechnol.* **2013**, 8, 933-938.
 66. Zhou, H.; Fan, Z.; Lemons, P. K.; Cheng, H. A Facile Approach to Functionalize Cell Membrane-Coated Nanoparticles. *Theranostics* **2016**, 6, 1012.
 67. Su, J. H.; Sun, H. P.; Meng, Q. S.; Yi, Q.; Zhang, P. C.; Zhang, Z. W.; Yu, H. J.; Li, Y. P. Bioinspired Nanoparticles with NIR-Controlled Drug Release for Synergetic Chemophotothermal Therapy of Metastatic Breast Cancer. *Adv. Funct. Mater.* **2016**, 26, 7495-7506.
 68. Zhang, P. F.; Liu, G.; Chen, X. Y. Nanobiotechnology: Cell Membrane-Based Delivery Systems. *Nano Today* **2016**, doi: 10.1016/j.nantod.2016.10.008.
 69. Fang, R. H.; Hu, C. M. J.; Chen, K. N. H.; Luk, B. T.; Carpenter, C. W.; Gao, W. W.; Li, S. L.; Zhang, D. E.; Lu, W. Y.; Zhang, L. F. Lipid-Insertion Enables Targeting Functionalization of Erythrocyte Membrane-Cloaked Nanoparticles. *Nanoscale* **2013**, 5, 8884-8888.
 70. Abdelmohesen, L. K. E. A.; Nijemeisland, M.; Pawar, G. M.; Janssen, G. J. A.; Nolte, R. J. M.; Van Hest, J. C. M.; Wilson, D. A. Dynamic Loading and Unloading of Proteins in Polymeric Stomatocytes: Formation of An Anzyme-loaded Supramolecular Nanomotor. *ACS Nano* **2016**, 10, 2652-2660.
 71. Wang, C.; Ye, Y. Q.; Hochu, G. M.; Sadeghifar, H.; Gu, Z. Enhanced Cancer Immunotherapy by Microneedle Patch-Assisted Delivery of Anti-PD1 Antibody. *Nano Lett.* **2016**, 16, 2334-2340.

72. Ye, Y. Q.; Yu, J. C.; Wang, C.; Nguyen, N. Y.; Walker, G. M.; Buse, J. B.; Gu, Z. Microneedles Integrated with Pancreatic Cells and Synthetic Glucose-Signal Amplifiers for Smart Insulin Delivery. *Adv. Mater.* **2016**, *28*, 3115-3121.
73. Vankayala, R.; Sagadevan, A.; Vijayaraghavan, P.; Kuo, C. L.; Hwang, K. C. Metal Nanoparticles Sensitize the Formation of Singlet Oxygen. *Angew. Chem. Int. Ed.* **2011**, *50*, 10640-10644.
74. Yu, C. Y. Y.; Xu, H.; Ji, S. L.; Kwok, R. T. K.; Lam, J. W. Y.; Li, X. L.; Krishnan, S.; Ding, D.; Tang, B. Z. Mitochondrion-Anchoring Photosensitizer with Aggregation-Induced Emission Characteristics Synergistically Boosts the Radiosensitivity of Cancer Cells to Ionizing Radiation. *Adv. Mater.* **2017**, *28*, doi: 10.1002/adma.201606167.
75. Li, S. Y.; Cheng, H.; Xie, B. R.; Qiu, W. X.; Song, L. L.; Zhuo, R. X.; Zhang, X. Z. A Ratiometric Theranostic Probe for Tumor Targeting Therapy and Self-Therapeutic Monitoring. *Biomaterials* **2016**, *104*, 297-309.
76. Li, S. Y.; Cheng, H.; Qiu, W. X.; Liu, L. L.; Chen, S.; Hu, Y.; Xie, B. R.; Li, B.; Zhang, X. Z. Protease-Activable Cell-Penetrating Peptide-Protoporphyrin Conjugate for Targeted Photodynamic Therapy *In Vivo*. *ACS Appl. Mater. interfaces* **2015**, *7*, 28319-28329.
77. Han, K.; Wang, S. B.; Lei, Q.; Zhu, J. Y.; Zhang, X. Z. Ratiometric Biosensor for Aggregation-Induced Emission-Guided Precise Photodynamic Therapy. *ACS Nano* **2015**, *9*, 10268-10277.
78. Seidl, C.; Ungelenk, J.; Zittel, E.; Bergfeldt, T.; Sleeman, J. P.; Schepers, U.; Feldmann, C. Tin Tungstate Nanoparticles: A Photosensitizer for Photodynamic Tumor Therapy. *ACS Nano* **2016**, *10*, 3149-3157.
79. Wang, S. H.; Riedinger, A.; Li, H. B.; Fu, C. H.; Liu, H. Y.; Li, L. L.; Liu, T. L.; Tan, P. F.; Barthel, M. J.; Pugliese, G.; Donato, F. D.; D'Abbusco, M. S.; Meng, T. W.; Manna, L.;

- Meng, H.; Pellegrino, T. Plasmonic Copper Sulfide Nanocrystals Exhibiting Near-Infrared Photothermal and Photodynamic Therapeutic Effects. *ACS Nano* **2015**, *9*, 1788-1800.
80. Gao, L.; Liu, R.; Gao, F. P.; Wang, Y. L.; Jiang, X. L.; Gao, X. Y. Plasmon-Mediated Generation of Reactive Oxygen Species from Near-Infrared Light Excited Gold Nanocages for Photodynamic Therapy *in Vitro*. *ACS Nano* **2014**, *8*, 7260-7271.
 81. Lv, G. X.; Guo, W. S.; Zhang, W.; Zhang, T. B.; Li, S. Y.; Chen, S. Z.; Eltahan, A. S.; Wang, D. L.; Wang, Y. Q.; Zhang, J. C.; Wang, P. C.; Chang, J.; Liang, X. J. Near-Infrared Emission CuInS/ZnS Quantum Dots: All-in-One Theranostic Nanomedicines with Intrinsic Fluorescence/Photoacoustic Imaging for Tumor Phototherapy. *ACS Nano* **2016**, *10*, 9637-9645.
 82. Liu, J.; Liu, Z.; Barrow, C. J.; Yang, W. R. Molecularly Engineered Graphene Surfaces for Sensing Applications: A Review. *Anal. Chim. Acta* **2015**, *859*, 1-19.
 83. Zhao, Y.; Luo, Z.; Li, M. H.; Qu, Q. Y.; Ma, X.; Yu, S. H.; Zhao, Y. L. A Preloaded Amorphous Calcium Carbonate/Doxorubicin@Silica Nanoreactor for pH-Responsive Delivery of an Anticancer Drug. *Angew. Chem. Int. Ed.* **2015**, *54*, 919-922.
 84. Mi, P.; Kokuryo, D.; Cabral, H.; Wu, H. L.; Terada, Y.; Saga, T.; Aoki, I.; Nishiyama, N.; Kataoka, K. A pH-Activatable Nanoparticle with Signal-Amplification Capabilities for Non-Invasive Imaging of Tumour Malignancy. *Nat. Nanotechnol.* **2016**, *11*, 724-730.
 85. Tapeinos, C.; Pandit, A. Physical, Chemical, and Biological Structures based on ROS-Sensitive Moieties that are Able to Respond to Oxidative Microenvironments. *Adv. Mater.* **2016**, *28*, 5553-5585.
 86. Zhang, C.; Bu, W. B.; Ni, D. L.; Zhang, S. J.; Li, Q.; Yao, Z. W.; Zhang, J. W.; Yao, H. L.; Wang, Z.; Shi, J. L. Synthesis of Iron Nanometallic Glasses and Their Application in Cancer Therapy by a Localized Fenton Reaction. *Angew. Chem. Int. Ed.* **2016**, *55*, 2101-2106.

87. Wang, Y. Z.; Xie, Y.; Li, J.; Peng, Z. H.; Sheinin, Y.; Zhou, J. P.; Oupick, D. Tumor-Penetrating Nanoparticles for Enhanced Anticancer Activity of Combined Photodynamic and Hypoxia-Activated Therapy. *ACS Nano* **2017**, *11*, 2227-2238.
88. Weissleder, R.; Kelly, K.; Sun, E. Y.; Shtatland, T.; Josephson, L. Cell-Specific Targeting of Nanoparticles by Multivalent Attachment of Small Molecules. *Nat. Biotechnol.* **2005**, *23*, 1418-1423.
89. Rabinovich, G. A.; Gabrilovich, D.; Sotomayor, E. M. Immunosuppressive Strategies that Are Mediated by Tumor Cells. *Annu. Rev. Immunol.* **2007**, *25*, 267-296.
90. Zhu, G.; Zhang, S.; Song, E.; Zheng, J.; Hu, R.; Fang, X.; Tan, W. Building Fluorescent DNA Nanodevices on Target Living Cell Surfaces. *Angew. Chem. Int. Ed.* **2013**, *52*, 5490-5496.
91. Ishiwata, H.; Suzuki, N.; Ando, S.; Kikuchi, H.; Kitagawa, T. Characteristics and Biodistribution of Cationic Liposomes and Their DNA Complexes. *J. Control. Release* **2000**, *69*, 139-148.
92. Neuberger, T.; Schöpf, B.; Hofmann, H.; Hofmann, M.; Von Rechenberg, B. Superparamagnetic Nanoparticles for Biomedical Applications: Possibilities and Limitations of a New Drug Delivery System. *J. Magn. Magn. Mater.* **2005**, *293*, 483-496.
93. Warburg, O.; Wind, F.; Negelein, E. The Metabolism of Tumors in the Body. *J. Gen. Physiol.* **1927**, *8*, 519-530.
94. Eguchi, Y.; Shimizu, S.; Tsujimoto, Y. Intracellular ATP Levels Determine Cell Death Fate by Apoptosis or Necrosis. *Cancer Res.* **1997**, *57*, 1835-1840.



Scheme 1. Schematic illustration of the cancer cell membrane camouflaged cascade bioreactor for cancer targeting starvation therapy and PDT. A) The preparation processes of mCGP. B) The immune escape and homotypic targeting abilities of mCGP endowing cancer accumulation and retention behaviors after intravenous injection. C) The cascade reactions would amplify the synergistic effects of mCGP to cut off the cancer cell glucose supply for starvation therapy and promote the 1O_2 generation for PDT under light irradiation.

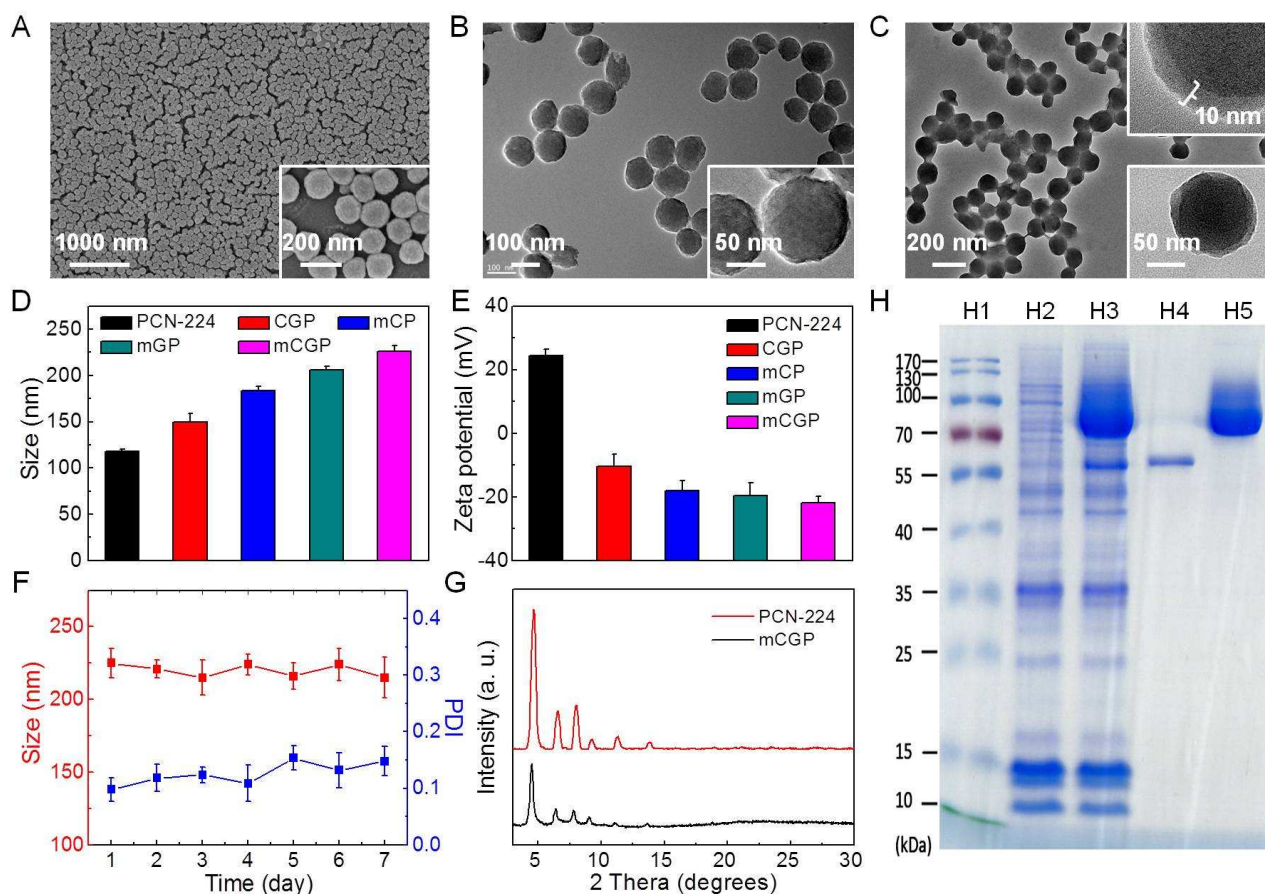


Figure 1. The characterizations of mCGP. A) SEM image and magnified SEM image (inserted) of PCN-224. B) TEM image and magnified TEM image (inserted) of PCN-224. C) TEM image and high-resolution TEM images (inserted) of mCGP. D) The hydrodynamic size distribution and E) the zeta potential of PCN-224, mCP, mGP and mCGP. F) The hydrodynamic size distribution and PDI changes of mCGP in 7 days. G) PXRD patterns of PCN-224 and mCGP. H) SDS-PAGE protein analysis of H1) marker, H2) 4T1 cell membrane, H3) mCGP, H4) catalase and H5) GOx.

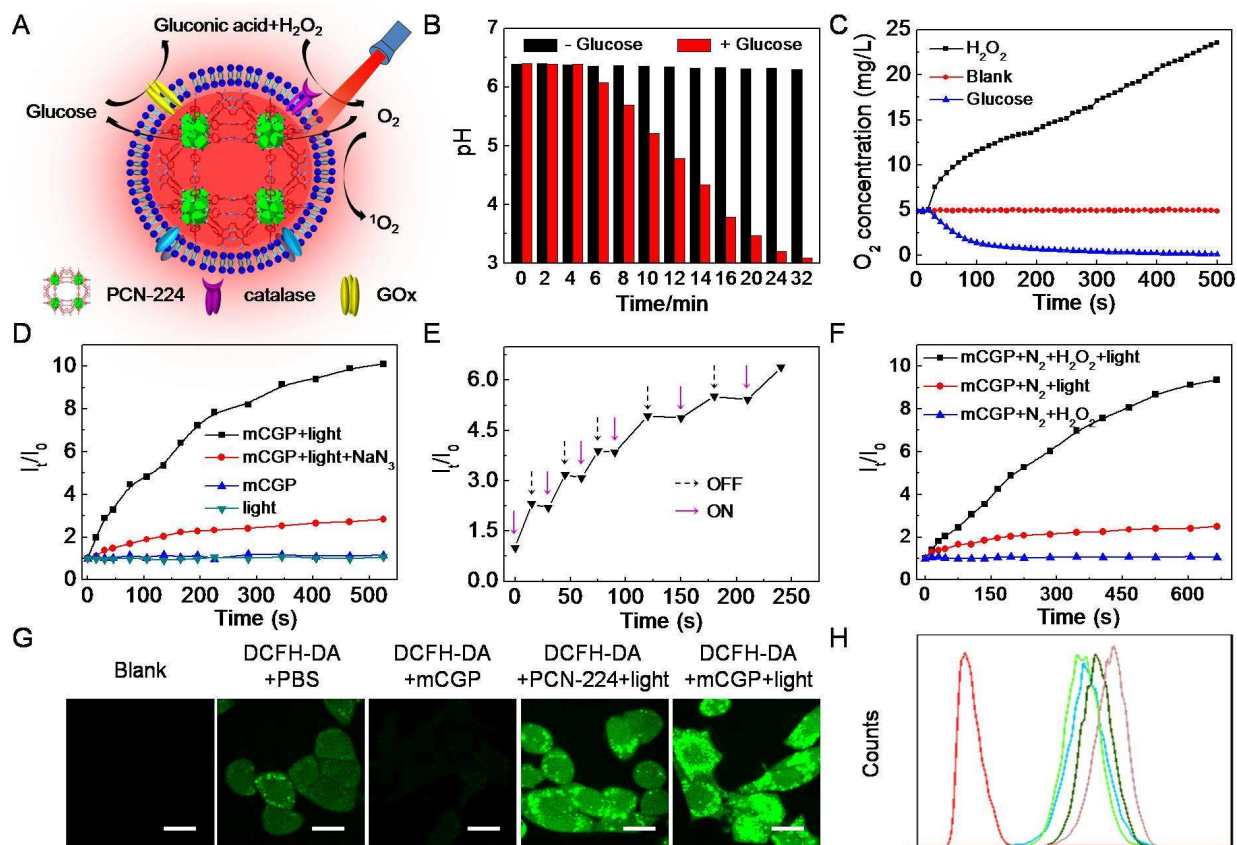


Figure 2. The cascade reactions in mCGP. A) Schematic illustration of the cascade reactions of mCGP including catalyzing the breakdown of H_2O_2 , decomposing glucose and producing 1O_2 . B) The pH values changes of mCGP solution in the absence and presence of glucose. C) The O_2 concentration changes of mCGP solution in the presence of H_2O_2 or glucose. D) The SOSG fluorescence changes in the presence of light, mCGP, mCGP and light or mCGP, light and NaN_3 . E) The SOSG fluorescence changes on the response of OFF-ON irradiation for mCGP. F) The SOSG fluorescence changes of SOSG in the absence of O_2 but in the presence of H_2O_2 , light, or H_2O_2 and light. G) CLSM images 4T1 cells with various treatments. Excitation wavelength: 488 nm, Emission wavelength: 515 ± 35 nm. Scale bar: 20 μm . H) flow cytometry analysis of 4T1 cells after treatment with DCFH-DA (cyan), DCFH-DA and mCGP (green), DCFH-DA, PCN-224 and light (black) or DCFH-DA, mCGP and light (wine).

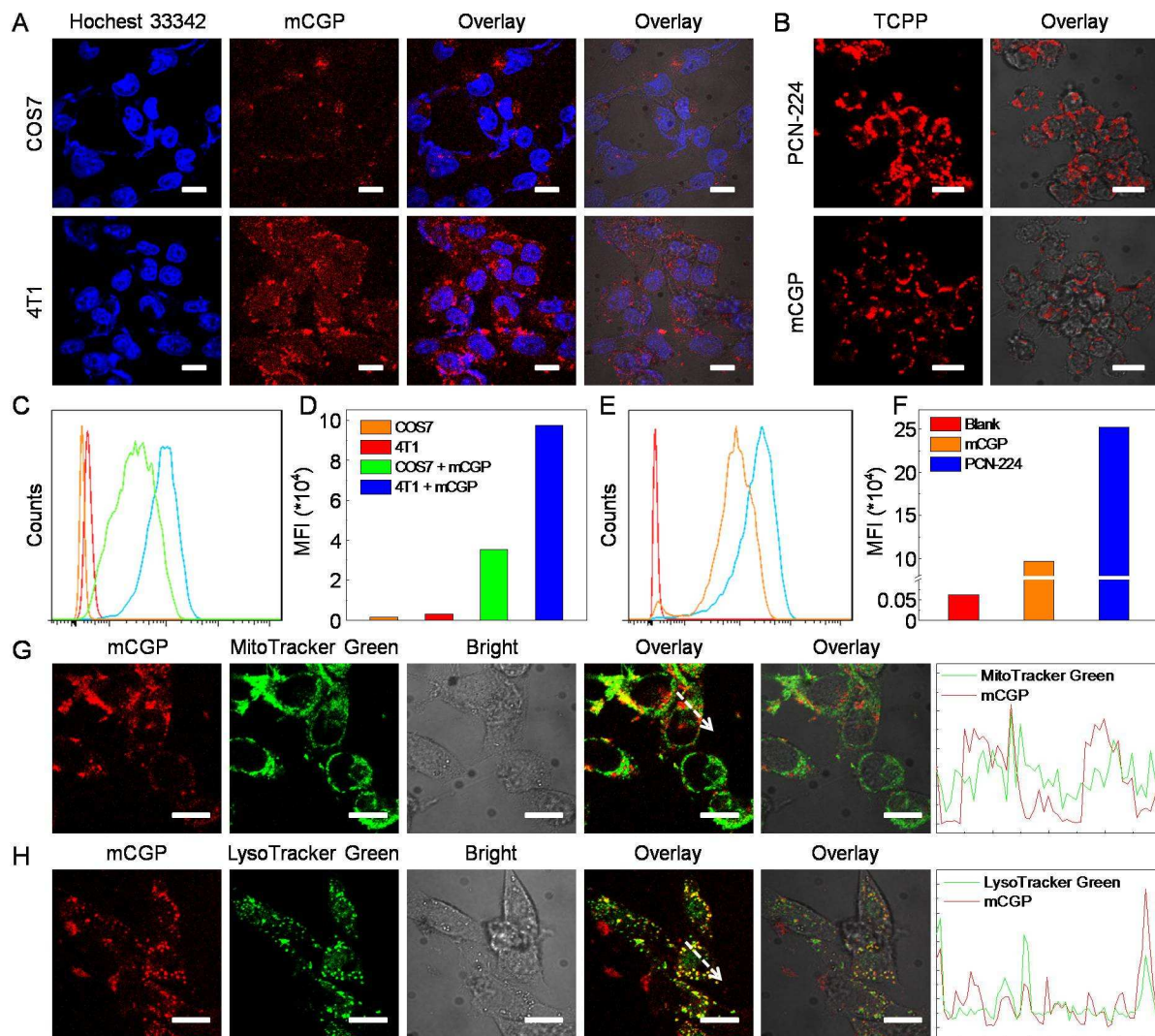


Figure 3. Homotypic targeting and immune escape abilities of mCGP. A) CLSM images of COS7 cells and 4T1 cells after treatment with mCGP and stained by Hoechst 33342. B) The CLSM images of RAW264.7 after treatment with PCN-224 or mCGP. C) Flow cytometry analysis of COS7 cells (green line) and 4T1 cells (cyan line) after treatment with mCGP using COS7 cells (yellow line) and 4T1 cells (red line) without any treatment as controls, and D) their corresponding mean fluorescence intensity (MFI) analysis. E) Flow cytometry analysis of RAW264.7 after treatment with PCN-224 (cyan line) or mCGP (yellow line) using RAW264.7 without any treatment as a control (red line), and F) their corresponding MFI analysis. CLSM images and the corresponding fluorescence intensity profile analysis (marked as arrow) of 4T1

cells after treatment with mCGP and stained by G) MitoTracker Green or H) LysoTracker Green. Scale bar: 20 μm . MitoTracker green and LysoTracker green: excitation wavelength: 488 nm, emission wavelength: 515 ± 35 nm; TCPP: excitation wavelength: 543 nm, emission wavelength: 650 ± 35 nm.

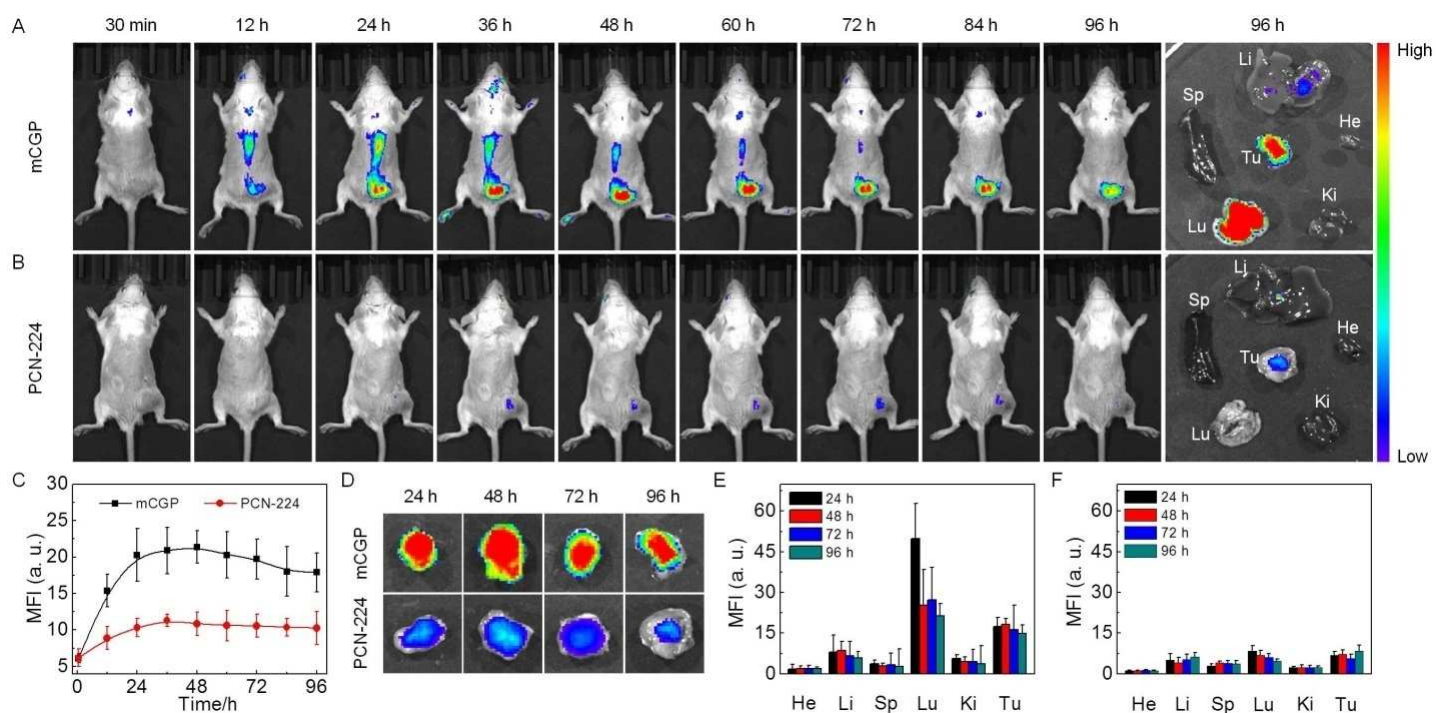


Figure 4. The cancer targeting and retention behaviors of mCNP. The *in vivo* and *ex vivo* fluorescence images of 4T1 cancer bearing mice after intravenously injection of A) mCNP or B) PCN-224 for various time intervals. C) Semiquantitative mean fluorescence intensity (MFI) analysis at the cancer site after intravenously injection for various time intervals. D) The fluorescence images of the sacrificed cancer tissues after intravenously injection for 24 h, 48 h, 72 h, 96 h. Semiquantitative MFI analysis of the major organs and cancer tissues after intravenously injection of E) mCNP or F) PCN-224 for various time. He, Li, Sp, Lu, Ki, and Tu stand for heart, liver, spleen, lung, kidney, and tumor, respectively.

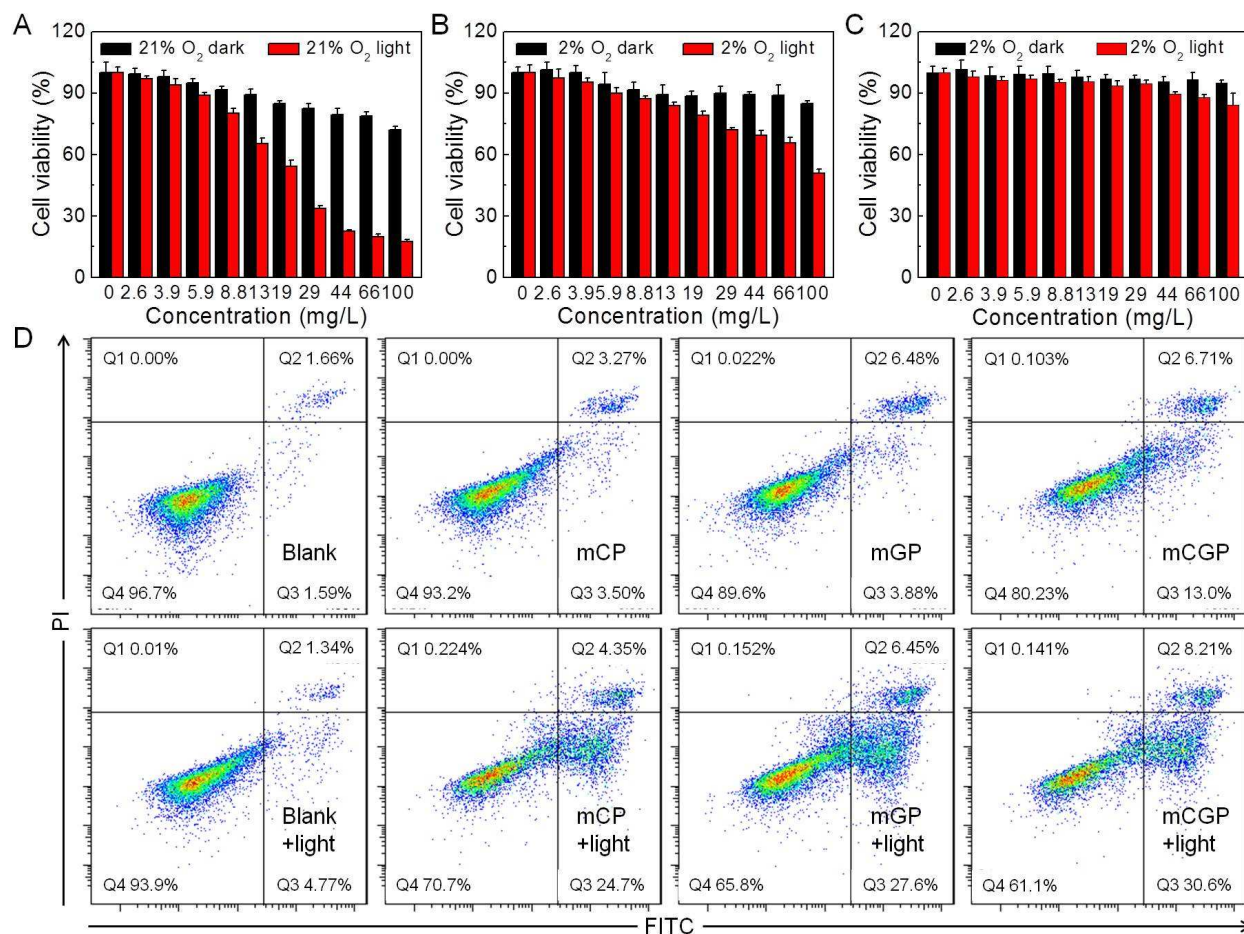


Figure 5. The synergistic stivation and PDT therapeutic effects of mCGP *in vitro*. The dark and light toxicities of mCGP against 4T1 cells by MTT assay under A) 21% O₂ or B) 2% O₂. C) Dark and light toxicities of mGP against 4T1 cells under 2% O₂. D) The dark and light toxicities of mCP, mGP and mCGP by flow cytometry analysis using 4T1 cells without any treatment as the blank control.

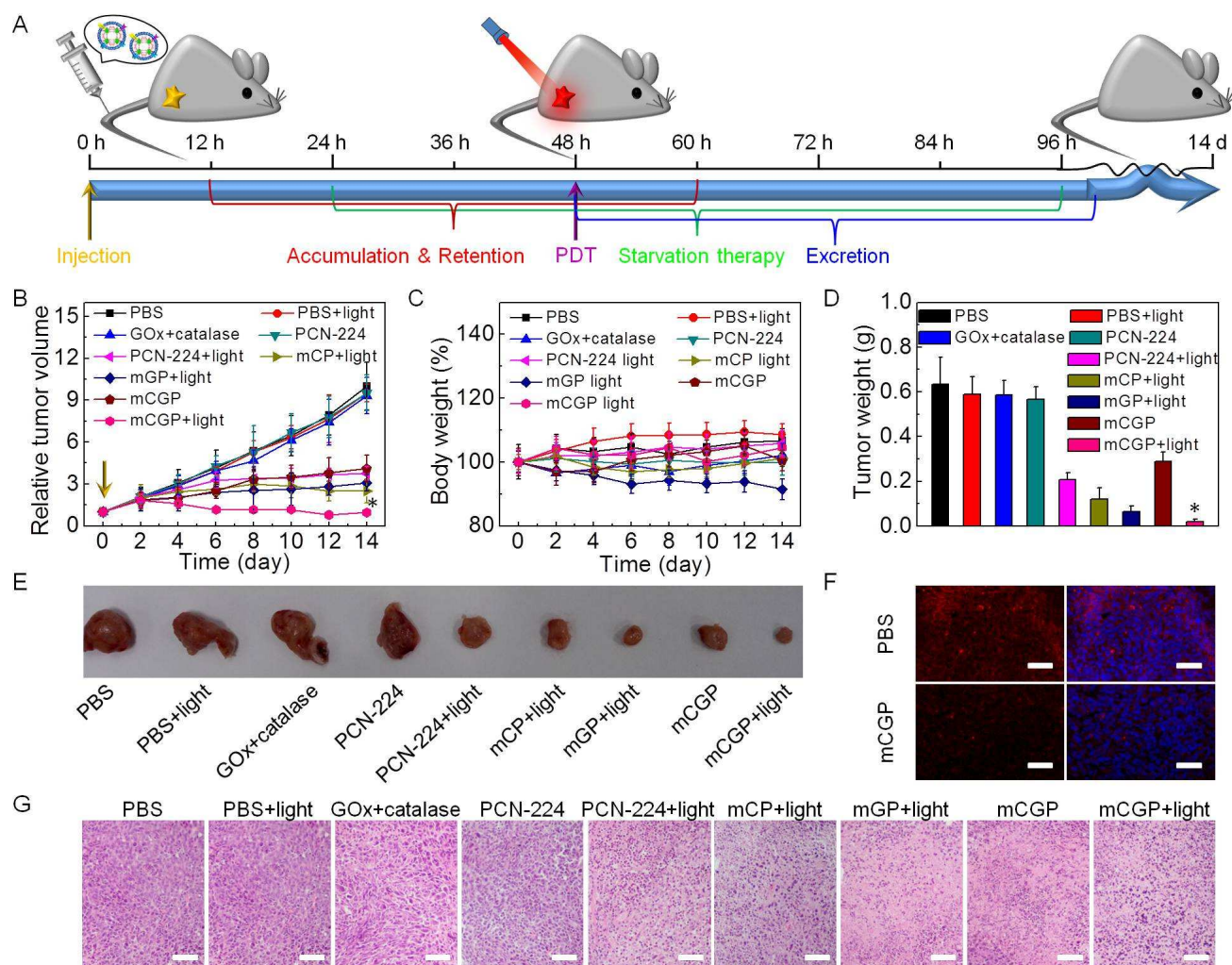


Figure 6. The anticancer efficiency of mCGP *in vivo*. A) Schematic illustration of the cancer targeting, retention and excretion behaviors as well as the synergistic starvation therapy and PDT of mCGP. B) The relative cancer volume and C) body weight changes in 14 days after various treatments, * $P < 0.05$. The arrow represented the administration time. D) The average cancer weight and E) representative cancer tissues after various treatments for 14 days, * $P < 0.05$. F) Immunofluorescence staining of HIF-1 α after treatment with PBS or mCGP. G) H&E staining of the sacrificed cancer tissues after various treatments for 14 days. Scale bar: 200 μ m.

TOC image

